



# Novel approach to investment casting of heat-resistant steel turbine blades for aircraft engines

Pei-Hsing Huang<sup>1</sup> · Leonard Kuo-Liang Shih<sup>1</sup> · Hung-Mao Lin<sup>2</sup> · Che-I Chu<sup>3</sup> · Chuen-Shii Chou<sup>3</sup>

Received: 3 May 2019 / Accepted: 17 July 2019 / Published online: 31 July 2019  
© Springer-Verlag London Ltd., part of Springer Nature 2019

## Abstract

Defects that form during the investment casting of turbine blades for aircraft engines pose a serious hazard to flight safety and greatly increase the costs associated with manufacturing. In this study, we conducted numerical simulations based on a retained melt modulus model to analyze the flow of metals through molds in order to determine the probability of shrinkage defect (PSD) in heat-resistant steel (SCH12) turbine blades for aircraft engines. The results of preliminary simulations and experiments were used to guide the establishment of simulations based on four casting schemes. Our objective in this stage was to identify the casting scheme with the lowest PSD. We then implemented the best of the four schemes with the bottom of the casting system immersed in cold water. We also incorporated virtual thermo-dynamical sensors in the simulations to characterize the effects of water depth on the rate and direction of solidification in the mold cavity. We then applied the optimal investment casting conditions to the fabrication of turbine blades in an established foundry. X-ray analysis detected almost none of the detrimental defects commonly associated with this type of casting, thereby demonstrating the efficacy of the proposed scheme.

**Keywords** Investment casting · Turbine blades · Retained melt modulus · Probability of shrinkage defects · Virtual thermo-dynamical sensor

## 1 Introduction

Turbine blades are key components in aircraft engines. High temperature differences and a harsh operating environment impose complex internal stresses within the blades. Long-term operation under these conditions can easily result in cavitation and the formation of surface cracks. Severe defects pose a hazard to safety and the need for regular replacement greatly inflates operating costs [1]. Researchers are constantly seeking methods by which to enhance the resistance of turbine

blades to high temperatures, while eliminating shrinkage and pore formation during investment casting [2, 3].

Investment casting is used in many industries requiring high precision in the creation of objects with complex shapes and smooth surfaces [4–8]. The process of fabricating turbine blades via investment casting is highly complex, due in part to the fact that shrinkage during casting is highly nonlinear [1–3]. Most previous studies on casting have employed trial-and-error methods, which tend to be imprecise, time-consuming, and expensive. One of the main problems is the fact that the flow of molten iron through the cavity and the direction of solidification cannot be observed, thereby making it difficult to make reasonable predictions pertaining to the formation of the casting defects. Figure 1 (a)–(d) present some of the defects typically observed in turbine blades fabricated via investment casting, including pore formation due to shrinkage between the inner-side of outer ring and the blade, notches in the blade due to insufficient material, and the overflow of molten iron on the back-side of the turbine blades. It is essential that designers have the capacity to make accurate predictions regarding shrinkage during the solidification process [1–3].

Advances in computer technology have enabled the use of computer-aided engineering software to predict where and

---

Submitted to The International Journal of Advanced Manufacturing Technology, April 2019; Revised, July 2019

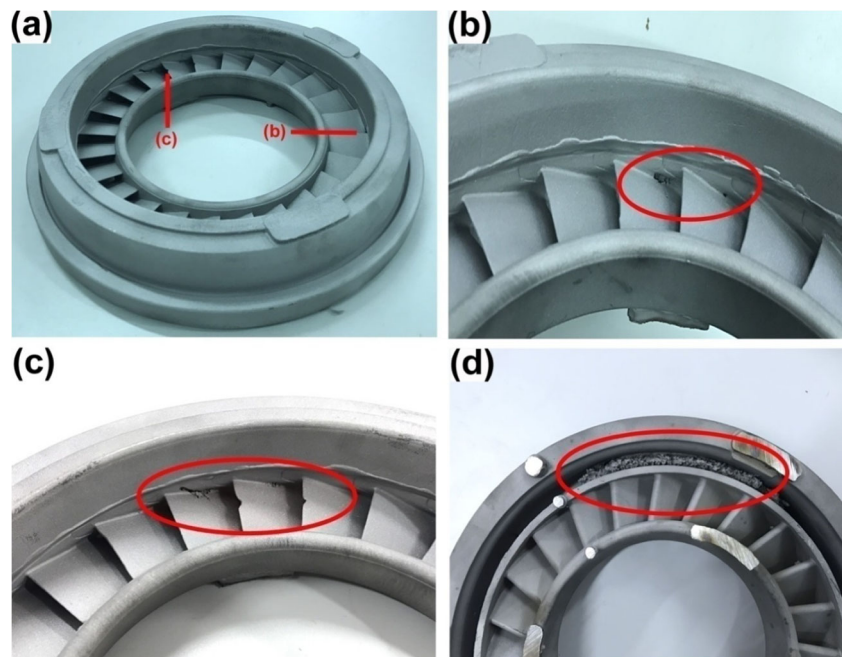
✉ Chuen-Shii Chou  
cschou@mail.npust.edu.tw

<sup>1</sup> Department of Mechanical Engineering, National Yunlin University of Science and Technology, Douliu, Yunlin 64002, Taiwan

<sup>2</sup> Department of Chemical and Materials Engineering, Southern Taiwan University of Science and Technology, Tainan 710, Taiwan

<sup>3</sup> Department of Mechanical Engineering, National Pingtung University of Science and Technology, Pingtung 912, Taiwan

**Fig. 1** Typical casting defects in turbine blades. (a) Indication of casting defects occurring in the turbine blades. (b) Shrinkage porosity between the inner-side of the outer ring and the blade. (c) Notch in the turbine blade. (d) The overflows of the molten iron on the back-side of the turbine blades



how defects are likely to form and the direction of solidification during casting, thereby eliminating many of the costs inherent in conventional trial-and-error methods. For example, ProCAST computer software was developed to investigate the dynamic temperature field and shrinkage porosity in casting [7]. It has been used by researchers to observe the flow of molten iron in the cavity and predict the position of casting defects [9]. It has also been used to eliminate shrinkage holes in the impeller of 200ZJA slurry pump [5]. It has even been used to examine investment casting die profiles through a reversing design method [10]. Other computer software (ANSYS) was used to study the reduction of residual stress in a cast during precision casting [11], and AnyCasting software was used to simulate the semi-solid thixoforming of Al-Cu-Mn-Ti alloy [12].

Dou et al. [10] used ProCAST to establish processing parameters for the investment casting of turbine blades. However, few previous studies have systematically investigated the optimization of investment casting and then carried out experiments to verify the efficacy of their numerical predictions. In this study, we conducted numerical simulations based on a retained melt modulus (RMM) model to analyze patterns in mold flow and predict where and how defects were likely to occur during the casting of heat-resistant steel (SCH12) turbine blades for aircraft engines. This study was conducted in four stages: (1) We compared our preliminary casting scheme (Case0) with experiment results obtained using a lost-wax investment casting process. (2) This analysis was then used to conduct simulations using four casting schemes: top gating system (Case1), bottom gating system (Case2), side gating system (Case3), and side gating systems with variations in size and geometry (Case4). (3) Numerical simulations were

conducted for each of the aforementioned casting systems under five test conditions (i.e., different ceramic shells and casting temperatures). We also conducted simulations in which the proposed scheme (with the bottom of the casting system immersed in cold water) was applied to Case4. (4) The optimal casting conditions derived in the simulations were then used in the fabrication of turbine blades via investment casting. Finally, X-ray analysis was used to assess the efficacy of the proposed scheme in avoiding casting defects.

## 2 Materials and method

### 2.1 Material properties

Turbine blades are made from SCH12 steel, which has a high chrome and nickel content with the following composition: C ( $\leq 0.2\sim 0.4\%$ ), Si ( $\leq 2.0\%$ ), Cr ( $18.0\sim 23.0\%$ ), Mn ( $\leq 2.0\%$ ), Ni ( $8.0\sim 12.0\%$ ), P ( $\leq 0.04\%$ ), and S ( $\leq 0.04\%$ ). This composition provides good resistance to corrosion and high temperatures as well as good mechanical properties. The thermo-physical properties of SCH12 steel are as follows: density ( $7.75 \text{ g/cm}^3$ ), specific heat ( $0.1198 \text{ cal/g } ^\circ\text{C}$ ), thermal conductivity ( $0.075 \text{ cal/s cm } ^\circ\text{C}$ ), latent heat ( $69.262 \text{ cal/g}$ ), liquid-phase temperature ( $1400 \text{ } ^\circ\text{C}$ ), and solid-phase temperature ( $1375 \text{ } ^\circ\text{C}$ ) [13]. Table 1 lists the test conditions for each of the casting systems assessed in this study. Five tests were conducted for each casting system under various ceramic shell temperatures ( $T_{\text{ceramic}}$ ) and casting temperatures ( $T_{\text{casting}}$ ), as listed in Table 1. In this study, we adopted gravity casting with air cooling (or water cooling) using shell molds made of zircon sand.

**Table 1** Experiment and simulation conditions for each of the casting schemes

	Exp1	Exp2	Exp3	Exp4	Exp5
Casting material	SCH 12				
Shell mold material	Zircon sand				
Mesh number	9000000				
$T_{\text{ceramic}}$ (°C)	1100	1150	1200	1200	1250
$T_{\text{casting}}$ (°C)	1500	1550	1600	1650	1650
$V_{\text{pouring}}$ (cm/s)	8				
$\delta$ (mm)	5.5				

$T_{\text{ceramic}}$ ,  $T_{\text{casting}}$ ,  $V_{\text{pouring}}$ , and  $\delta$  represent temperature of ceramic shell, temperature of casting, pouring velocity, and shell thickness, respectively

### 2.2 Numerical model

We conducted simulations on the investment casting of turbine blades using the AnyCasting software package. Hexahedral elements of appropriate size were used to mesh the investment casting systems. Calculations pertaining to the pressure field, velocity field, and temperature field during filling and solidification were based on the continuity equation, Navier–Stokes equation, energy conservation, the volume of fluid (VOF) function, and  $k$ - $\varepsilon$  equations [13–15], as follows.

The following continuity equation was used to calculate the mass conservation of molten metal into the cavity during the filling process:

$$\frac{\partial \rho}{\partial t} + \nabla \cdot (\rho \vec{u}) = 0 \tag{1}$$

In Eq. (1),  $\rho$  and  $t$  respectively denote fluid density and progressive time, and  $\vec{u}$  indicates the velocity vector.

The Navier–stokes equation was used to calculate pressure and velocity fields of molten metal, as follows:

$$\rho \frac{\partial \vec{u}}{\partial t} + \rho \vec{u} \cdot \nabla \vec{u} = -\nabla P + \mu \nabla^2 \vec{u} + \rho \vec{g} \tag{2}$$

In Eq. (2),  $P$ ,  $\mu$ , and  $\vec{g}$  respectively represent the pressure, dynamic viscosity of molten metal, and gravitational acceleration.

The energy conservation equation was used to calculate temperature field and solidification process of the molten metal, as follows:

$$\rho \frac{\partial H}{\partial t} + \rho H \nabla \cdot \vec{u} - \nabla \cdot (k \nabla T) - q = 0 \tag{3}$$

In Eq. (3),  $H$  and  $q$  respectively represent enthalpy and volumetric heat flux.

The volume function equation was used in conjunction with the Navier–stokes equation to determine the flow patterns of molten metal in the non-fixed direction at the free boundary, as follows:

$$\frac{\partial F_v}{\partial t} + \vec{u} \cdot \nabla F_v = 0 \tag{4}$$

In Eq. (4),  $F_v$  represents the volume-of-fluid function. When a calculation cell was empty (i.e., no fluid inside), the  $F_v$  value was set at zero, and when a cell was full, the  $F_v$  value was equal to 1 [13, 15].

Conventional  $k$ - $\varepsilon$  equations were used to take into account the evolution of turbulent flow, as follows:

$$\frac{\partial k_e}{\partial t} + u_j \frac{\partial k_e}{\partial x_j} = \frac{\partial}{\partial x_j} \left[ \left( u + \frac{u_t}{\sigma_k} \right) \frac{\partial k_e}{\partial x_j} \right] + P_{ke} - \varepsilon \tag{5}$$

$$\frac{\partial \varepsilon}{\partial t} + u_j \frac{\partial \varepsilon}{\partial x_j} = \frac{\partial}{\partial x_j} \left[ \left( u + \frac{u_t}{\sigma_\varepsilon} \right) \frac{\partial \varepsilon}{\partial x_j} \right] + c_{\varepsilon 1} P_k \frac{\varepsilon}{k_e} - c_{\varepsilon 2} \frac{\varepsilon^2}{k_e} \tag{6}$$

In Eqs. (5) and (6),  $u_j$ ,  $\varepsilon$ , and  $k_e$  respectively represent velocity components in the corresponding direction, the dissipation rate of turbulence kinetic energy, and turbulence kinetic energy. Symbols  $\sigma_k$  and  $\sigma_\varepsilon$  respectively represent Prandtl numbers corresponding to turbulence kinetic energy ( $k_e$ ) and the rate of dissipation ( $\varepsilon$ ). In Eqs. (5) and (6),  $u_t$  represents turbulence eddy viscosity, given by

$$u_t = \frac{\rho C_\mu k_e^2}{\varepsilon} \tag{7}$$

In Eqs. (5)–(7), the values of the constants used in the turbulence model were as follows:  $C_\mu = 0.09$ ,  $\sigma_k = 1.00$ ,  $\sigma_\varepsilon = 1.30$ ,  $C_{\varepsilon 1} = 1.44$ , and  $C_{\varepsilon 2} = 1.92$  [13].

For each casting system, a statistical RMM model was used to evaluate the probability of shrinkage cavity formation, as follows [13, 16, 17]:

$$M_R = V_R / S_R \tag{8}$$

In Eq. (8),  $V_R$  and  $S_R$  respectively represent the volume and surface area of isolated melt at the time that each mesh reached the critical solid fraction. A smaller RMM value corresponds to a higher likelihood of defect formation [13, 16].

The dynamic and solidification behaviors of the molten metal in the cavity were determined using Eqs. (1)–(8). When using AnyCasting to solve differential equations and analyze the mold flow, we selected the finite difference method, due to its superiority over other numerical methods in terms of convergence speed and iterative computation. Convergence tests were used to determine the optimal number of grids in the casting system (approximately 9,000,000 elements).

### 3 Results and discussion

#### 3.1 Preliminary casting scheme (Case0)

Figure 2 presents a schematic illustration showing the gating system used to cast the turbine blades in Case0, where molten metal poured into the sprue cup and flowed into the transverse runner and mold cavity. The air that was originally in the cavity was forced out of the vent hole to release the pressure within the gating system. The dimensions of gating system in Case0 were as follows: 90.5 mm (diameter of sprue cup) and 47 mm (L) × 17 mm (W) (size of ingate). In our numerical simulations, we adopted the test conditions in Exp3, which are commonly used in the manufacture of turbine blades in domestic foundries.

Figure 3 (a)–(d) illustrate the probability of shrinkage defect (PSD) distribution in the gating systems, as determined using the RMM model under Case0-Exp3, as follows: (a) isometric view, (b) front cross-sectional view, (c) top cross-sectional view of the inner ring and blades, and (d) top cross-sectional view of the outer ring and blades. The probabilistic defect parameter, defined as the product of the rate of shrinkage during solidification and the casting constant [18], was dimensionless with a value ranging from 1.0 (highest likelihood) shown in red to 0.0 (lowest likelihood) shown in blue. Figure 3 (a) reveals the casting defects that appeared at the outer ring as well as at the junction between the turbine blade and inner ring. This phenomenon was also observed in Fig. 3(b)–(d), wherein the PSD exceeded 0.55. These effects can be attributed to the profound difference in geometry between the turbine blade and the inner ring, which could easily lead to the formation of a geometrical thermal node.

Figure 4 (a)–(f) present photographs of casting defects in experiments used to verify the results obtained under Case0-Exp3, as follows: (a) indication of a defect on the front-side of the turbine blade, (b) enlarged image of the surface shrinkage porosity defects on the outer-side of the outer ring, (c)

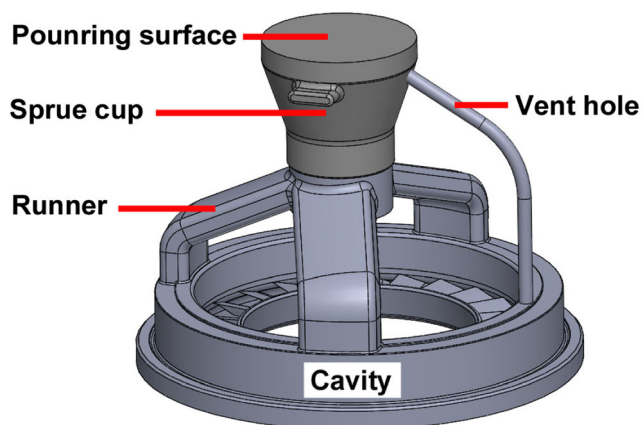


**Fig. 2** Schematic of gating system design based on Fig. 1 (i.e., the casting scheme in Case0)

enlarged image of insufficient pour defects on the blades, (d) indication of defect on the back-side of the turbine blade, (e) surface shrinkage porosity defects at junction between the blades and inner ring, and (f) enlarged image of surface shrinkage porosity defects and overflows of the molten iron on the inner-side of the outer ring.

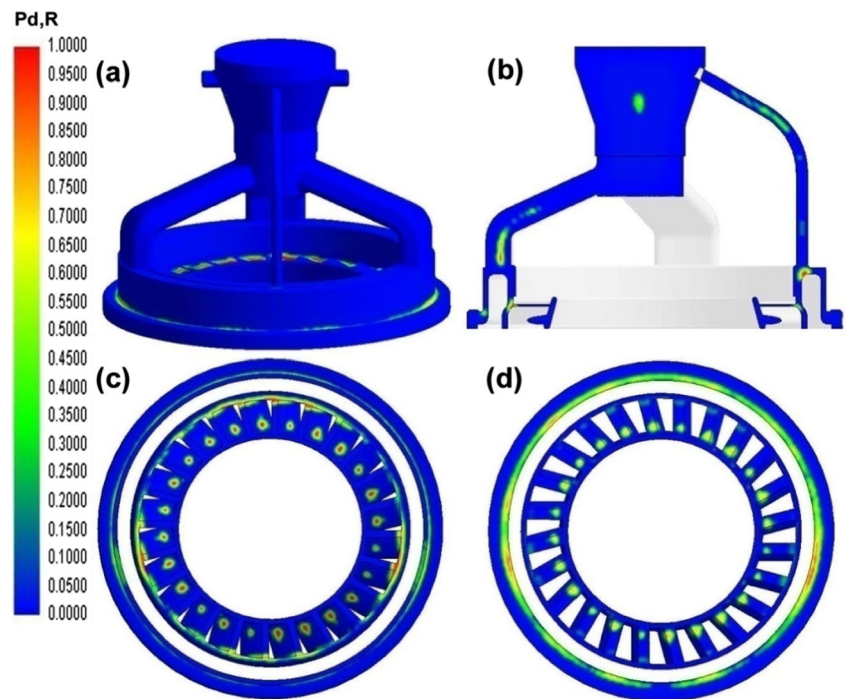
These casting defects can be explained by the following. (1) Insufficient feed from runners during solidification resulted in the formation of shrinkage porosity defects in the isolated retained melt, as shown in Fig. 4 (b) and (f). (2) Portions of the sand shell peeled off during the casting process, with the result that a portion of the molten iron overflowed the mold, resulted in insufficient pour at the corresponding blade, as shown in Fig. 4(c). (3) During the solidification process, the molten iron may be blocked between the inner ring and the ingate, and the shrinkage of isolated residual melts significantly increased the value of PSD at the junction between the blades and inner ring (Fig. 4(e)). As a result, the casting defects of turbine blade shown in the experimental results (Fig. 4) are consistent with those found in Fig. 3 obtained from numerical simulations.

#### 3.2 Evolution of design concepts for proposed casting schemes (Case1~Case4)

This study proposed four systems for casting turbine blades; the underlying design concepts of which are as follows. (1) In Case1, we used a top gating system, in which the ingates were respectively set at the outer ring, the inner ring, and the inner cone to eliminate shrinkage defects at the outer ring and at the junction between the turbine blade and inner ring; both of which were observed in Case0. (2) In Case2, we used a bottom gating system with the cross gate to buffer the movement of molten iron through the runner, thereby ensuring that the molten iron flowed stably into the cavity (i.e., without turbulence). Three risers were also set at the outer ring to replenish the residual melt. (3) In Case3, we used a side gating system with the ingates arranged at the inner ring and risers arranged at the outer ring, to simultaneously replenish the residual melt in the inner and outer rings. Interestingly, the arrangement of risers close to the sprue cup was shown to suppress the cooling rate of the molten iron, which improved the feeding effect. (4) In Case4, we modified a side gating system (Case3) in which the size and geometry of the gating system were altered to increase the strength and avoid overlapping of the ceramic shell. Figure 5 (a)–(d) respectively present illustrations of the gating systems in Case1, Case2, Case3, and Case4. To ensure a reasonable comparison with the results obtained under Case0-Exp3, all numerical simulations of the proposed casting systems were conducted using test conditions related to Exp3.



**Fig. 3** PSD distribution of the gating system under Case0-Exp3. (a) Isometric view. (b) Front cross-sectional view. (c) Top cross-sectional view of the inner ring and blades. (d) Top cross-sectional view of the outer ring and blades



### 3.3 Numerical simulations in Case1 to Case4

Figure 6 (a)–(d) present the PSD distribution of the gating system under Case1-Exp3, as follows: (a) isometric view, (b) front cross-sectional view, (c) top cross-sectional view of the inner and outer rings and blades, and (d) top cross-sectional

view of the bottom of the turbine blades. As shown in Fig. 6 (a) and (b), higher PSD values appeared at the junction between the inner ring and turbine blade, which matched the trend observed in Case0-Exp3. However, we observed higher PSD values at the bottom of the turbine blades, as shown in Fig. 6 (c) and (d).

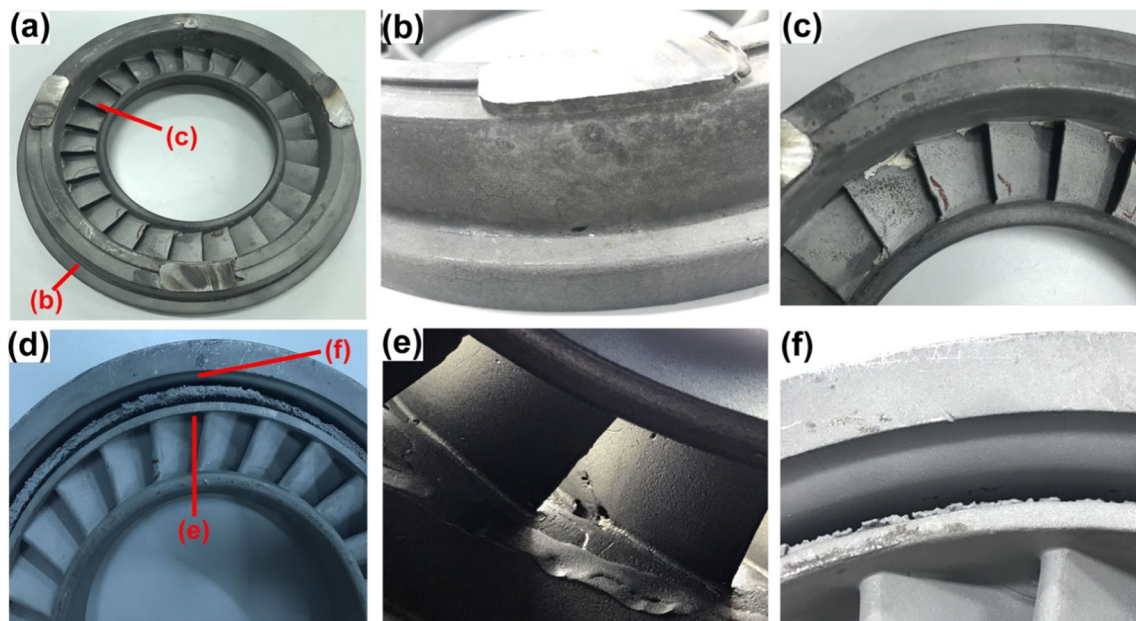


**Fig. 4** Photographs of casting defects in experimental verification under Case0-Exp3. (a) Indication of defect occurring on the front-side of the turbine blade. (b) Enlarged image of the surface shrinkage porosity defects on the outer-side of the outer ring. (c) Enlarged image of insufficient pour defects on the blade. (d) Indication of defect occurring

on the back-side of turbine blade. (e) Surface shrinkage porosity defects at the junction between the blades and inner ring. (f) Enlarged image of surface shrinkage porosity defects and overflows of the molten iron on the inner-side of the outer ring

**Fig. 5** Illustrations of the gating systems. (a) Case1. (b) Case2. (c) Case3. (d) Case4

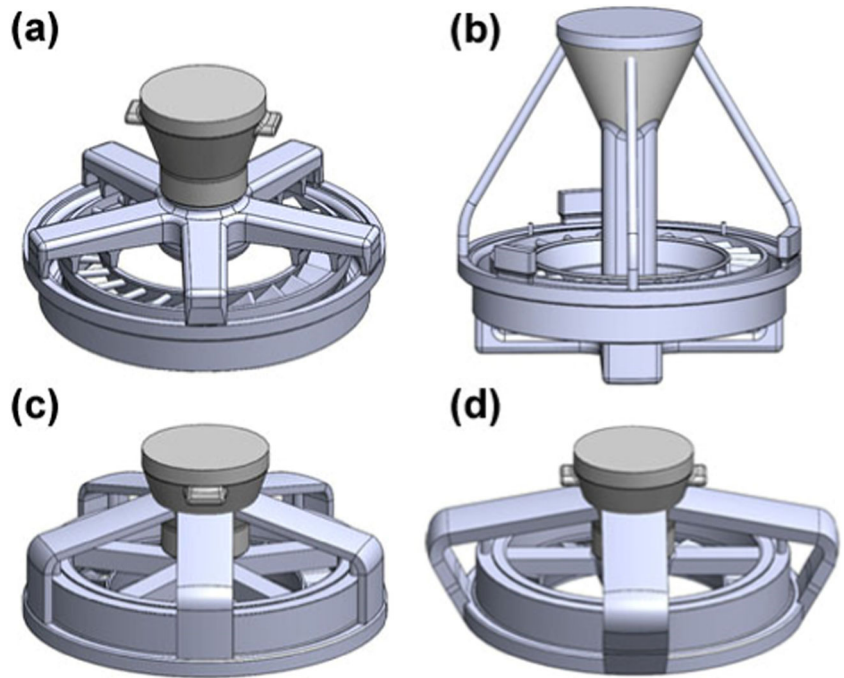
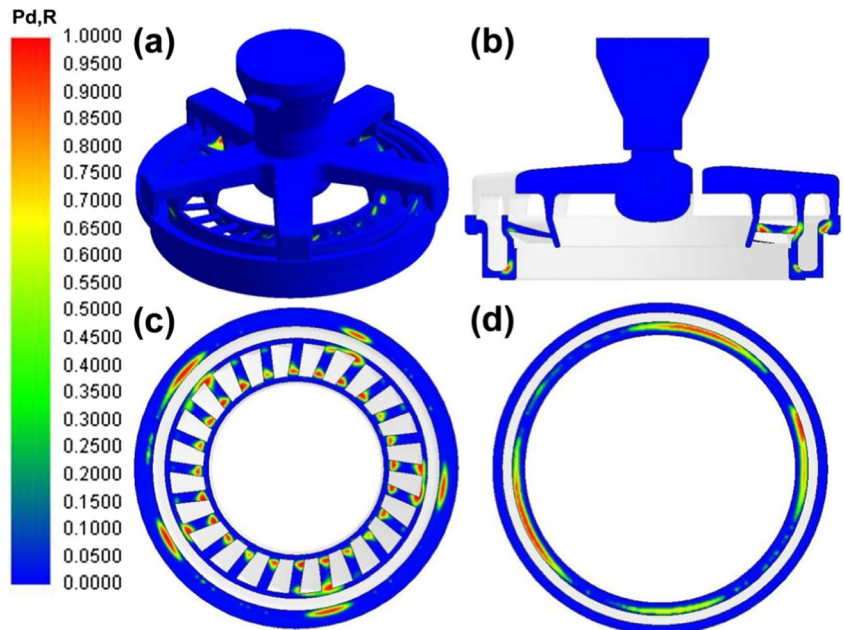


Figure 7 (a)–(d) present the PSD distributions of the gating system under Case2-Exp3, as follows: (a) isometric view, (b) front cross-sectional view, (c) top cross-sectional view of the inner ring, and (d) top cross-sectional view of the outer ring. Casting defects appeared at the outer ring and at the junction between the turbine blade and inner ring, as shown in Fig. 7 (c) and (d). This can be attributed to the fact that the cooling rate of molten iron in the riser exceeded the cooling rate in other parts of the gating system during the solidification process, with the result that the solidification of molten iron in the

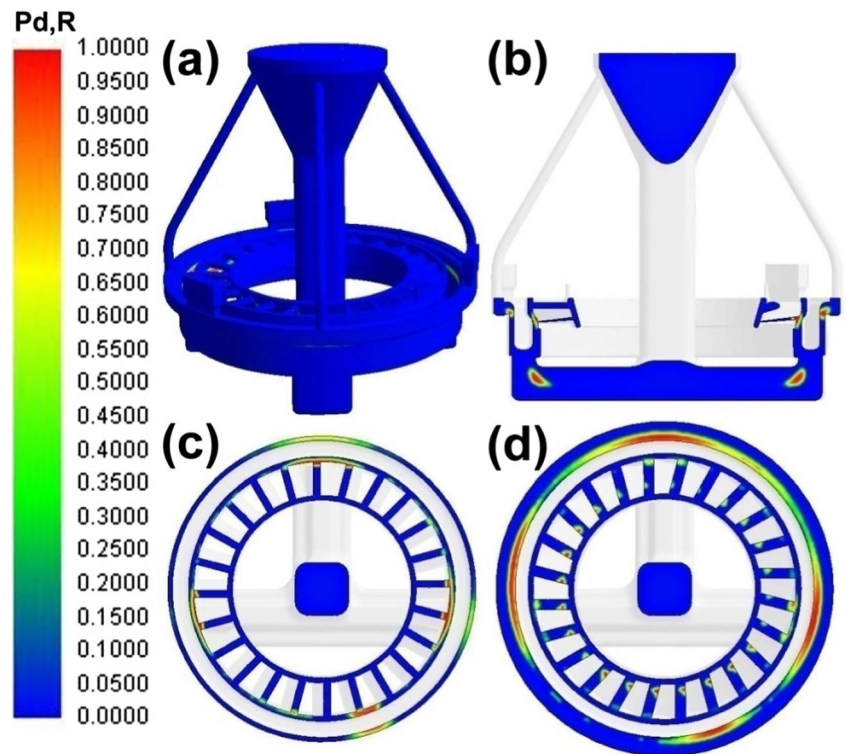
riser occurred earlier, thereby nullifying the feeding efficacy of the riser.

Figure 8 (a)–(d) present the PSD distributions of the gating system under Case3-Exp3, as follows: (a) isometric view, (b) front cross-sectional view, (c) top cross-sectional view of the inner ring, and (d) top cross-sectional view of the outer ring. Under Case3-Exp3, the combination of a side gating system with ingates at the inner ring and risers at the outer ring greatly reduced the PSD values observed at the outer ring and at the junction between the turbine blade and inner ring in Case0,

**Fig. 6** PSD distribution of the gating system under Case1-Exp3. (a) Isometric view. (b) Front cross-sectional view. (c) Top cross-sectional view of the inner and outer rings and blades. (d) Top cross-sectional view of the bottom of the turbine blades



**Fig. 7** PSD distribution of the gating system under Case2-Exp3. (a) Isometric view. (b) Front cross-sectional view. (c) Top cross-sectional view of the inner ring. (d) Top cross-sectional view of the outer ring



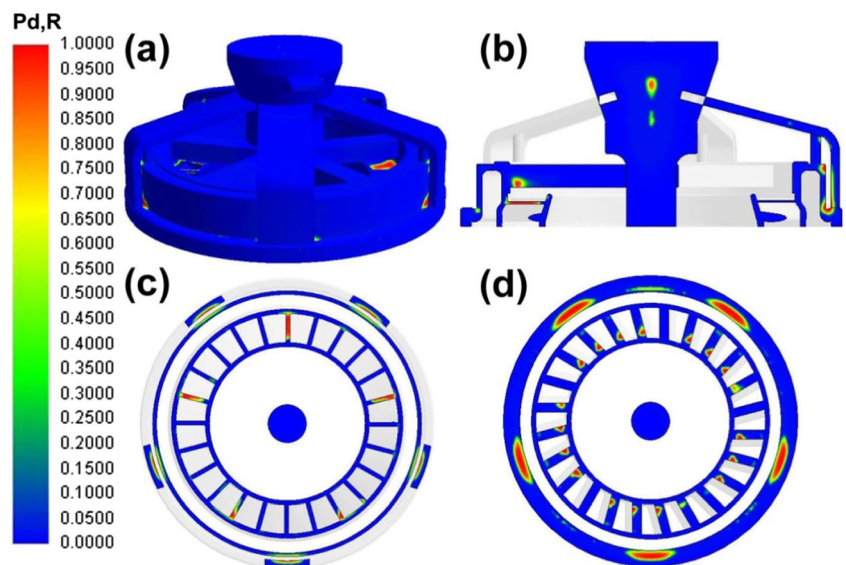
Case1, and Case2. However, we obtained higher PSD values at the outer wall of the riser, due to the fact that the thickness of the ceramic shell was not specified in the simulations, which led to overlapping.

Figure 9 (a)–(d) present the PSD distributions of the gating system under Case4-Exp3, as follows: (a) isometric view, (b) front cross-sectional view, (c) top cross-sectional view of the inner ring, and (d) top cross-sectional view of the outer ring. Case4-Exp3 (in which the side gating system (Case3) was modified by changing size of the ingate and the angle of the riser)

proved effective in reducing the PSD values at the outer ring and at the junction between the turbine blade and inner ring as well as at the outer wall of the riser.

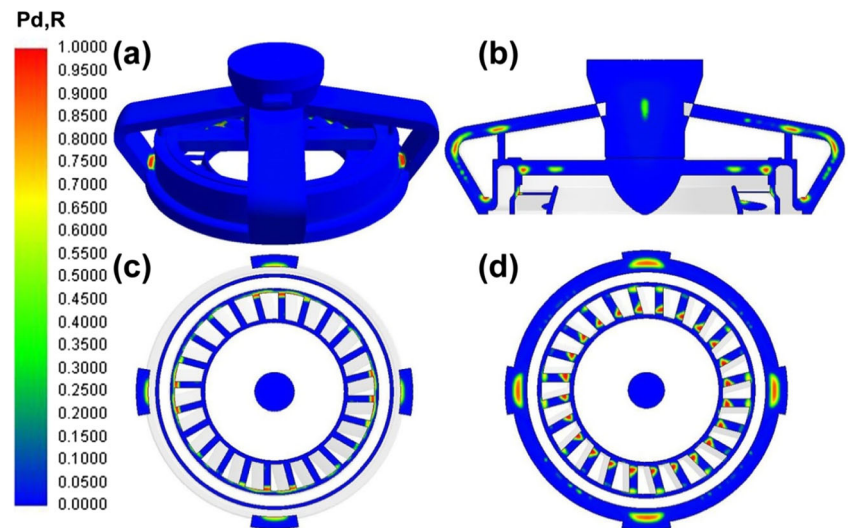
Figure 10 (a)–(d) respectively present the PSD distributions of the gating systems under Case4-Exp1, Case4-Exp2, Case4-Exp4, and Case4-Exp5. Figure 10 (a)–(d) respectively present three images: front cross-sectional view of the gating system (left), top cross-sectional view of the inner ring (center), and top cross-sectional view of the outer ring (right). The highest PSD value at the outer ring and at the junction between the turbine

**Fig. 8** PSD distribution of the gating system under Case3-Exp3. (a) Isometric view. (b) Front cross-sectional view. (c) Top cross-sectional view of the inner ring. (d) Top cross-sectional view of the outer ring

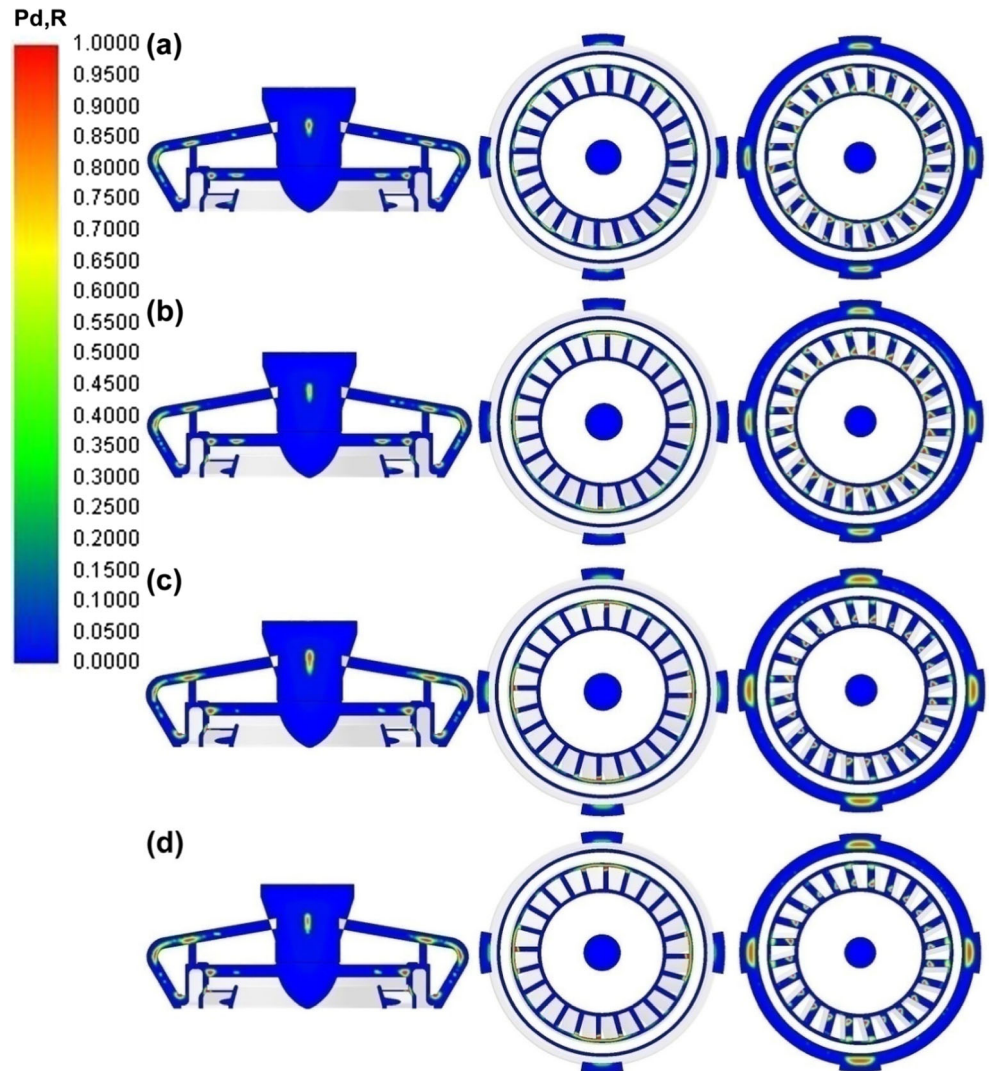




**Fig. 9** PSD distribution of the gating system under Case4-Exp3. (a) Isometric view. (b) Front cross-sectional view. (c) Top cross-sectional view of the inner ring. (d) Top cross-sectional view of the outer ring



**Fig. 10** PSD distributions under Case4 with four various test conditions. (a) Exp1. (b) Exp2. (c) Exp4. (d) Exp5. Each row illustrates three images: front cross-sectional view of the gating system (left), top cross-sectional view of the inner ring (center), and top cross-sectional view of the outer ring (right)





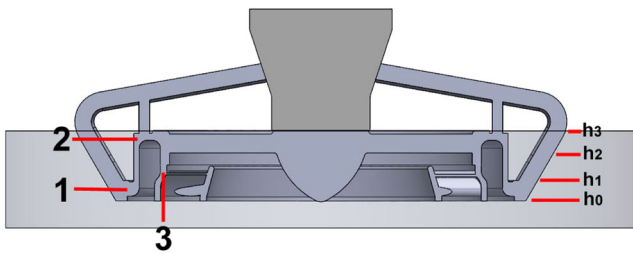


**Fig. 11** Illustrations of the gating system under Case4-Exp1 soaked in cold water with various depths ( $h_0 = 0$  mm,  $h_1 = 13$  mm,  $h_2 = 26$  mm, and  $h_3 = 44.5$  mm) as well as the position of virtual thermo-dynamical sensors (from (1) to (3))

blade and inner ring (close to 1) was obtained under Case4-Exp3 (Fig. 9(c), (d)). Decreasing the temperature of the ceramic shell from 1200 to 1100 °C and decreasing the temperature of the casting from 1600 to 1500 °C lowered the highest PSD value in these areas to < 0.5 under Case4-Exp1 (Fig. 10(a)). In the following section, we sought to eliminate the PSD from the turbine blades by implementing simulations under Case4-Exp1 conditions but with a novel cooling strategy in which the bottom of the casting system was immersed in cold water.

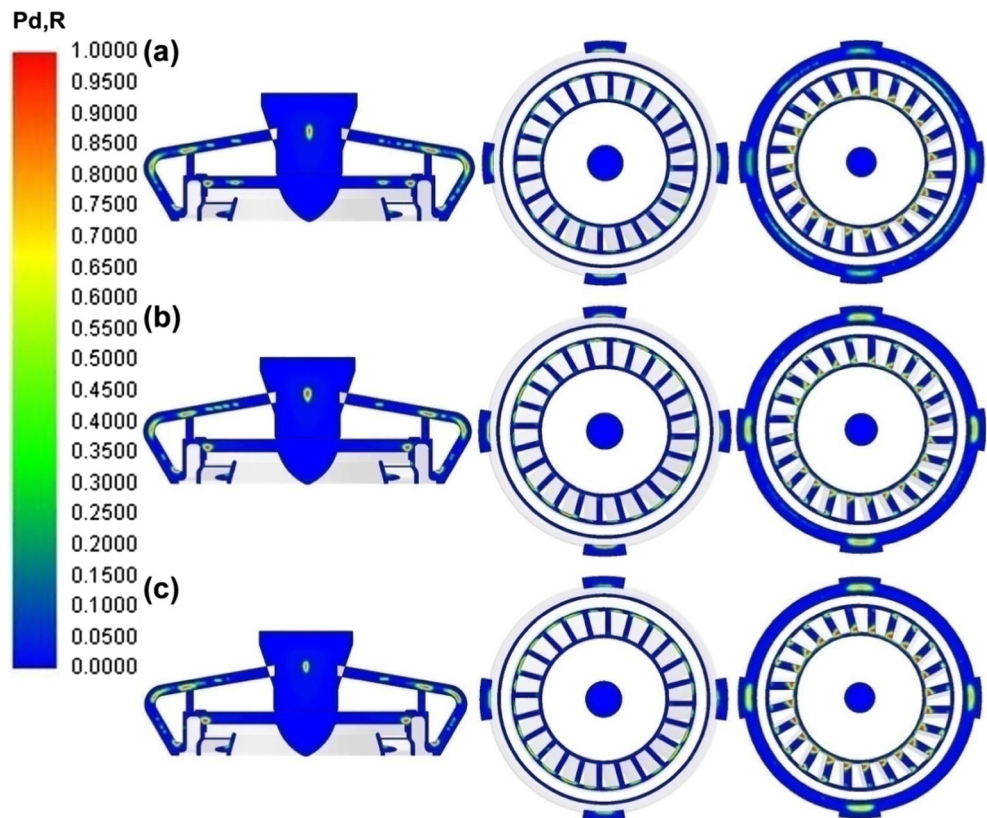
### 3.4 Numerical simulations in Case4-Exp1 with novel cooling strategy

Figure 11 presents the gating system under Case4-Exp1, while immersed in cold water of various depths:  $h_0$  (0 mm),  $h_1$  (13

mm),  $h_2$  (26 mm), and  $h_3$  (44.5 mm). The position of virtual thermo-dynamic sensors (TDSs) is indicated by numbers (1) to (3) in Fig. 11, corresponding to regions associated with higher PSD values. Figure 12 (a)–(c) respectively present the PSD distributions under Case4-Exp1 with three depths of cold water (13, 26, and 44.5 mm). Each figure presents the following three images: front cross-sectional view of the gating system (left), top cross-sectional view of the inner ring (center), and top cross-sectional view of the outer ring (right). There was a tremendous reduction in the PSD value at the outer ring and at the junction between the turbine blade and inner ring when using a water depth of 13 mm (Fig. 12(a)), compared with the PSD values obtained using the preliminary gating system (Case0-Exp3), as shown in Fig. 3(b)–(d), as well as the casting scheme under Case4-Exp1 (Fig. 10(a)). This can be attributed to the fact that 13 mm of water was sufficient to alter the solidification direction and suppress the formation of isolated residual melt. In comparison, immersing the mold more deeply (26 or 44.5 mm) enhanced only the solidification speed of the molten iron.

Figure 13 (a)–(d) respectively present the variations in temperature at TDS as a function of time under Case4-Exp1 with 4 immersion depths (0, 13, 26, and 44.5 mm). Each figure presents three curves: a red curve (TDS1, at the outer ring), a blue curve (TDS2, at the exterior of the casting), and a green curve (TDS3, at the junction between the turbine blade and inner ring). The results shown in Fig. 13(a)–(d) reveal the

**Fig. 12** PSD distributions under Case4-Exp1 with 3 depths of cold water: (a) 13 mm, (b) 26 mm, and (c) 44.5 mm. Each row illustrates three images: front cross-sectional view of the gating system (left), top cross-sectional view of the inner ring (center), and top cross-sectional view of the outer ring (right)



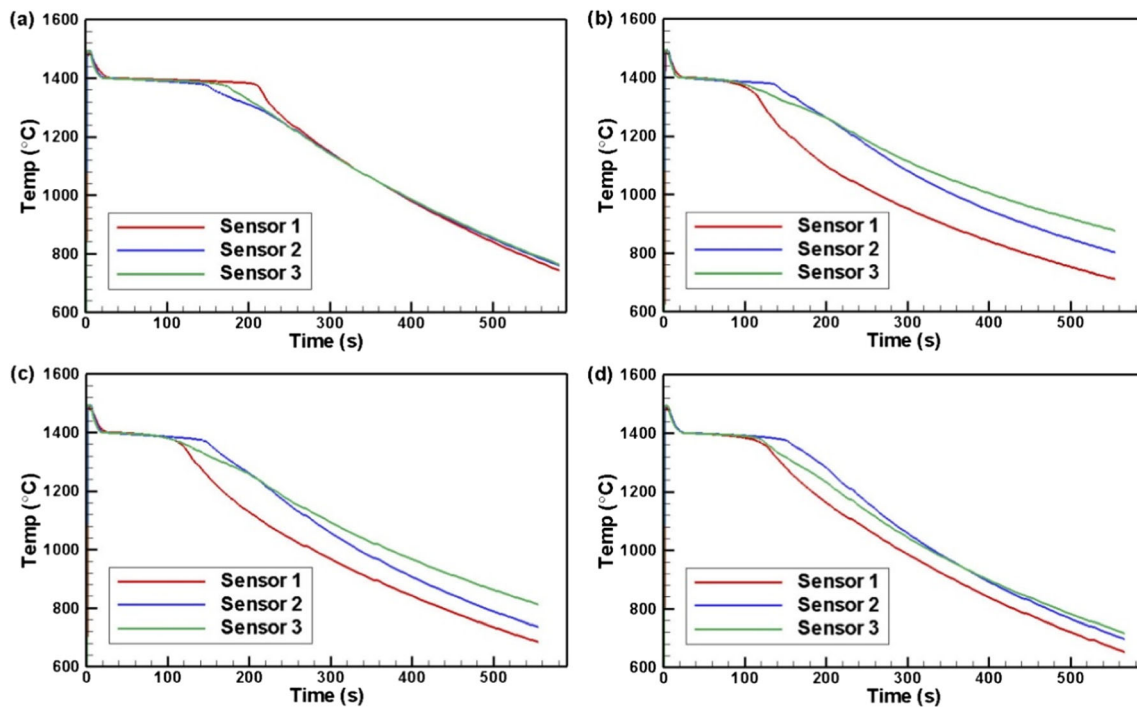


**Fig. 13** Variations in temperature at TDS with time in Case4-Exp1 with 4 immersion depths of cold water: (a) 0 mm, (b) 13 mm, (c) 26 mm, (d) 44.5 mm

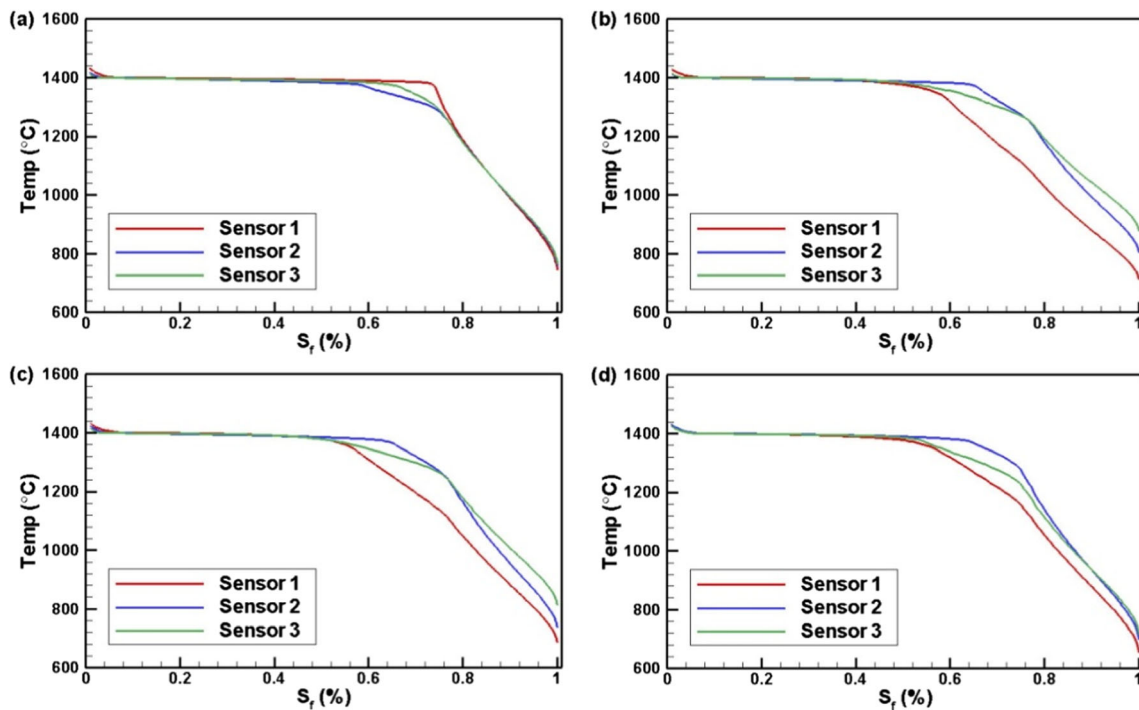
following important findings. (1) With an immersion depth of 0 mm, the time required for molten iron to reach the solidus temperature of the alloy (1375 °C) at each TDS was as follows: 140 s (TDS2), 160 s (TDS3), and 220 s (TDS1). After 300 s, no significant difference in temperature was observed among the TDSs, as shown in Fig. 13(a). (2) With an immersion depth of 13 mm, the temperature of the outer ring (TDS1) was the first to drop to 1375 °C at 80 s. The molten iron reached 1375 °C at 100 s at TDS3 and at 140 s at TDS2. After 200 s, TDS1 presented the lowest temperature, whereas TDS3 presented the highest temperature. (3) With an immersion depth of 26 mm, we observed a higher cooling rate at the outer and inner rings, with the result that the time required for molten iron to reach 1375 °C at TDS3 and TDS1 dropped to 80 s. After 100 s, there was only a negligible temperature difference between TDS3 and TDS1 (Fig. 13(c)), compared with the notable difference obtained when using an immersion depth of 13 mm (Fig. 13(b)). (4) An immersion depth of 44.5 mm increased the cooling rate of the entire casting, such that there was only a negligible temperature difference among the three TDSs.

Figure 14 (a)–(d) respectively present the variations in temperature at the TDS associated with the solidification fraction ( $S_f$ ) under Case4-Exp1 with 4 various immersion depths (0, 13, 26, and 44.5 mm). Each figure presents three curves indicating the three TDSs. The results in Fig. 14(a)–(d) reveal the following important findings. (1) With an immersion depth of 0 mm, the rate of solidification was highest in the exterior of casting, followed by the inner ring with the slowest at the outer

ring. As a result, the molten iron was blocked between the outer ring and the inner ring, which resulted in isolated residual melt and higher PSD values. (2) With an immersion depth of 13 mm, when the value of  $S_f$  exceeded 80%, the rate of solidification was highest at the outer ring, followed by the exterior of the casting, with the slowest at the inner ring, which established the direction of solidification throughout the entire casting from the outside to the inside. This prevented the blocking of molten iron and improved the feeding effect, which lowered the PSD values. (3) With an immersion depth of 26 or 44.5 mm, the rate of cooling throughout the entire casting was enhanced; however, there was only a negligible difference in solidification speed between the outer ring, the exterior of the casting, and the inner ring. As a result, there was no clear trend in the direction of solidification. The results in Figs. 13 and 14 (based on TDS measurements) provide valuable insight into the formation of shrinkage defects in turbine blades during investment casting.

### 3.5 Experimental verification under Case4-Exp1 with 13-mm soaking depth

Figure 15 (a)–(d) present photographs of samples fabricated to verify the simulation results obtained under Case4-Exp1 with an immersion depth of 13 mm: (a) finished product of casting with runners, (b) enlarged image showing the outer ring of the turbine blade, (c) enlarged image showing the junction between the blades and inner ring, and (d) finished turbine blade. Figure 16 (a) and (b) present X-ray images of experimental



**Fig. 14** Variations in temperature at TDS with the solidification fraction in Case4-Exp1 with 4 immersion depths of cold water: (a) 0 mm, (b) 13 mm, (c) 26 mm, (d) 44.5 mm

verification under Case4-Exp1 with 13-mm soaking depth for the outer ring of the turbine blade. Figure 16 (c) and (d) present X-ray images of samples fabricated to verify the simulation results under Case4-Exp1 with an immersion depth of 13 mm. Note that the X-rays were obtained from the blades and inner ring. No obvious shrinkage defects were observed in the

finished product, as shown in Fig. 15(b)–(d). Furthermore, no black spots were detected inside the turbine blades using non-destructive X-ray detection, as shown in Fig. 16(a)–(d). The quality of the finished heat-resistant steel (SCH12) turbine blades provides evidence supporting the efficacy of our strategy for the casting of turbine blades.

**Fig. 15** Photographs of experimental verification under Case4-Exp1 with an immersion depth of 13 mm. (a) Finished product of casting with runners. (b) Enlarged image showing the outer ring of the turbine blade. (c) Enlarged image showing the junction between the blades and inner ring. (d) Finished turbine blade

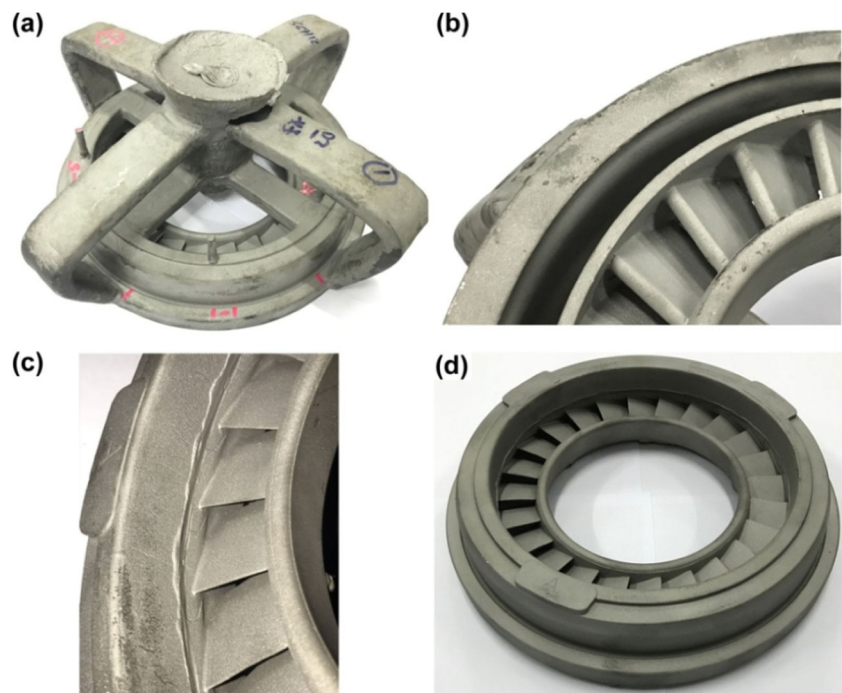
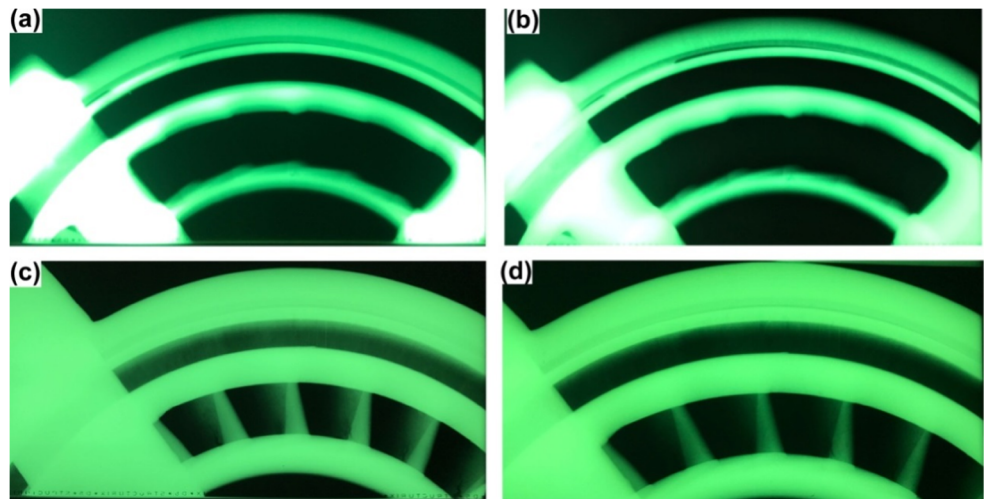




**Fig. 16** X-ray images of experimental verification under Case4-Exp1 with a 13-mm soaking depth. (a), (b) The outer ring of the turbine blade. (c), (d) The blades and inner ring



## 4 Conclusion

In this study, we conducted numerical simulations based on an RMM model to investigate where and how shrinkage defects are likely to form in heat-resistant steel (SCH12) turbine blades for aircraft engines. Our results obtained from the preliminary simulations and experiments were used to formulate four casting schemes for simulation, from which the scheme with the smallest PSD was selected for further improvement. We employed virtual TDSs in subsequent simulations of the casting system, with the aim of characterizing the rates and directions of solidification in various regions of the casting while immersed in cold water. Our numerical results reveal that a side gating system (Case4-Exp1) immersed in cold water could reduce the likelihood of casting defects. In this study, the optimal immersion depth was approximately 13 mm from the bottom of the casting system. We then applied the optimal casting conditions to the fabrication of turbine blades for an aircraft engine in a domestic foundry. X-rays reveal that the proposed casting scheme and pre-determined casting parameters eliminated most of the detrimental casting defects commonly associated with this type of casting procedure. The strategy presented in this paper provides a valuable reference for the investment casting of turbine blades for aircraft engines from the perspective of quality as well as cost efficiency.

**Funding information** The authors gratefully acknowledge the support provided for this research by the Ministry of Science and Technology, R.O.C. under grants MOST 107-2221-E-224-060 and MOST 107-2622-E-224-013-CC3.

## References

- Kuo JK, Huang PH, Lai HY, Chen JR (2017) Optimal gating system design for investment casting of 17-4PH stainless steel enclosed impeller by numerical simulation and experimental verification. *Int J Adv Manuf Technol* 92:1093–1103
- Dong YW, Li XL, Zhao Q, Yang J, Dao M (2017) Modeling of shrinkage during investment casting of thin-walled hollow turbine blades. *J Mater Process Technol* 244:190–203
- Huang PH, Guo MJ (2015) A study on the investment casting of 17-4PH stainless steel helical impeller of centrifugal pump. *Mater Res Innov* 19(S9):77–81
- Huang PH, Kuo JK, Guo MJ (2017) Removal of Cr Mo alloy steel components from investment casting gating system using vibration-excited fatigue failure. *Int J Adv Manuf Technol* 89:101–111
- Zhi XH, Han YJ, Yuan XM (2015) Casting process optimization for the impeller of 200ZJA slurry pump. *Int J Adv Manuf Technol* 77:1703–1710
- Huang PH, Wang BT, Chen YT (2014) An effective method for separating casting components from the runner system using vibration-induced fatigue damage. *Int J Adv Manuf Technol* 74:1275–1282
- Hou YH, Cheng ZQ, Feng WC, Liu BS (2007) Using Procast to forecast and analysis of the shrinkage porosity and its technical optimization swaminathan. *China Water Transport* 7(3):67–69
- Huang PH, Wu WJ, Shieh CH (2016) Compute-aided design of low pressure die-casting process of A356 aluminum wheels. *Appl Mech Mater* 864:173–178
- Zhou JH, Sun CB, Shang W, Li B (2013) The application research of simulation technology in investment casting process. *Mater Sci Technol* 21(5):109–112
- Dou YQ, Bu K, Dou YL, Dong YW (2010) Reversing design methodology of investment casting die profile based on ProCAST. *China Foundry* 7(2):132–137
- Keste AA, Gawande SH, Sarkar C (2016) Design optimization of precision casting for residual stress reduction. *J Comput Design Eng* 3(2):140–150
- Wang P, Cui JZ, Lu GM (2007) Semi-solid thixoforming simulation of Al-Cu-Mn-Ti alloy parts via AnyCasting. *Mater Northeastern Univ* 23(3):359–362
- User manual of AnyCasting. version 6.0
- Kuo JK, Huang PH, Lai HY, Wu WJ (2010) Design of casting systems for stainless steel exhaust manifold based on defective prediction model and experimental verification. *Int J Adv Manuf Technol* 100:529–540
- Hirt CW, Nichols BD (1981) Volume of fluid (VOF) method for the dynamics of free boundaries. *J Comp Phys* 39:201–225
- Kim KH, Hwang JH, Oh JS, Lee DH, Kim IH, Yoon YC (2007) Prediction of shrinkage defect in steel casting for marine engine

- cylinder cover by numerical analysis. Hyundai Industrial Research Institute, Hyundai Heavy Industries Co., Ulsan, pp 1–9
17. Huang PH, Lin CJ (2015) Computer-aided modeling and experimental verification of optimal gating system design for investment casting of precision rotor. *Int J Adv Manuf Technol* 79:997–1006
  18. Kim KH, Hwang JH, Oh JS, Lee DH, Kim IH, Yoon YC (2005) Prediction of shrinkage defect in steel casting for marine engine cylinder cover by numerical analysis. *World Foundry Congress (WFC06)* 209:1–9

**Publisher's note** Springer Nature remains neutral with regard to jurisdictional claims in published maps and institutional affiliations.